Title
THE MUON, AN EXOTIC PROBE OF SOLIDS

Author
Crowe, K.M.

Publication Date
1983-10-01

LBL-16725
Preprint

Lawrence Berkeley Laboratory
UNIVERSITY OF CALIFORNIA

Submitted to the Journal of Solid State Chemistry

THE MUON, AN EXOTIC PROBE OF SOLIDS

K.M. Crowe

October 1983

Prepared for the U.S. Department of Energy under Contract DE-AC03-76SF00098

DISCLAIMER

LBL-16725

THE MUON, AN EXOTIC PROBE OF SOLIDS

K. M. Crowe

Department of Physics and Lawrence Berkeley Laboratory
University of California, Berkeley, CA 94720

October 1983

This work was supported in part by the U.S. Department of Energy under Contracts DE-AC03-76SF00098, W-7405-ENG-36, and AT03-81ER40004.

LBL-16725

THE MUON, AN EXOTIC PROBE OF SOLIDS

K. M. Crowe

Department of Physics and Lawrence Berkeley Laboratory
University of California, Berkeley, CA 94720

ABSTRACT

A brief review of the μ SR technique, some of the successes, complications, and mysteries will be given. The comparison with other probes will be emphasized and hints of possible future work will be presented.

Precise determination of the vacuum properties of muons, its mass, its decay reaction, polarization, magnetic movement, its hydrogen-like $\mu^+ + e^-$ atom, Mu, and its hyperfine structure, and the energy levels of negative muonic atoms have been made extensively over the past 30 years. Table I shows the present status of these properties. The understanding of the relaxation of μ^+ spin in condensed media has in the recent decade been developed to the stage where new information about the properties of the media are beginning to appear. In a few cases because of the unique properties of the μ^+, the extreme case of a dilute probe, and its mass between the proton and position, phenomena have appeared in which well known theories can be tested in different regions. For example, the mobility of μ^+ in metals can be compared to hydrogen, Knight shifts can be measured and compared with simple theory. Magnetic fields at phase changes critical point fluctuations and spin glasses can be probed with the muons spin. The states of Mu in semiconductors are another example of new phenomenology which is being studied.

The list of examples is extensive and I have only mentioned those which are of personal interest. Figure 1 shows an enlarged scope of the subjects currently under investigation. For a more detailed review of the subject there are several reviews and documents which are available for study. (1)

The objective in this tutorial will be to outline the method with particular attention to the new techniques to provide an experimental foundation for the non-experts in the audience. I will attempt to anticipate some of the obvious questions and with a few examples and

a few proposed experiments I hope to introduce you to the jargon and lore which has evolved which unfortunately tends to make the literature difficult to master even for the specialists.

High quality intense sources of muons are available at the Meson facilities that produce pions. The decay of pion to μ^+ and neutrino produces longitudinal polarized muons due to maximum parity violation of the weak interaction coupling which is involved. When one restricts the decay kinematics to select muons from a narrow cone in the pion rest frame, the resulting μ^+ beam will be essentially completely polarized. Muons produced by decay in flight along the pion beam trajectories can be selected magnetically corresponding to foward or backward decays. Those muons arising from decay in the immediate vicinity of the primary beam target are called cloud muons and are only partically polarized. On the other hand, if muons come from pions which come to rest close to the outside surfaces of the production target, the muons are 100% polarized and these are called surface Arizona beams. The term Arizona beam is named for their inventors (2) from the University of Arizona. These have close to the maximum momentum in the 2 Body decay $\pi \rightarrow \mu + \nu$ at rest. Their range in material is about 200 milligrams/cm^2, which sometimes limits the application due to the target windows. However, for many low density gases and especially small targets, this beam is abundently well suited. The beam is transported to the users target with a magnetic channel and again fortunately there is no depolarization in transit ($g_\mu \simeq 2$) or in the slowing down process via atomic electric fields as the spin remains essentially undisturbed

from its initial polarization direction. Recently with the addition of strong transverse electostatic fields with crossed magnetic field (mass or wien filter) the spin can be rotated to produce a transverse polarized beam. This beam has the possibility for injection into a high longitudinal field (> 20 kg) without any significiant loss of polarization.

The muon decays into an electron and two neutrinos and the energy distribution for the positron is shown in Fig. 2.

$$\frac{dN(\omega,\theta)}{d\omega d\Omega} = \frac{\omega^2}{2\pi}\left[(3 - 2\omega) - \xi(1 - 2\omega)\cos\theta\right] = \frac{C}{2\pi}\left[1 + D\cos\theta\right] \quad (1)$$

where $\omega = E/E_{max}$ and θ is the angle of the electron from the muon spin momentum.

The targets in which the μ^+ stops therefore, can be in external magnetic fields with the axis either transverse or longitudinal to the muon spin direction. The precession in these fields lead to transverse, longitudinal, zero and High, (TF, LF, ZF, HF) rotation of the spin. This precession can be monitored due to the higly anisotropic beta decay of the μ^+. If one places an array of counters surrounding the muon stopping volume and records the time of the decay, the accumulated elapsed time histogram has wiggles which follow the evolution of the spin.

In summary the spectra of TF and HF can be represented as follows

$$dN(t)/dt = N_o\exp(-t/\tau_\mu)\{1 + A(t)\cos[\omega^\mu t + \phi]\} + BG \quad (2)$$

where τ_μ is the lifetime of the muon A(t) is the asymmetry amplitude which may be time dependent ω^μ is the precession frequency, and ϕ is a geometric phase angle associated with the detector. BG is the

background. Figure 3 shows the relation between the μ^+ spin and the finite detector. A typical μSR spectrometer is shown in Fig. 4. Table II gives the frequencies which the free muon would precess at different local fields. The frequency for muon precession at the same fields is also given.

$$\omega^{\mu} = \mu_{\mu} B/\hbar = g_{\mu}\mu_{o}^{\mu} B/\hbar = g_{\mu} eB/2m_{\mu}c$$
$$|\nu^{\mu}| = \frac{2\mu_{\mu} B}{h} = \frac{g_{\mu} eB}{4\pi m_{\mu} c} = 13.55 \frac{kHz}{G} \times |B| \qquad (3)$$

We must discuss several points here.

μ^+ vs μ^-. Both are interesting although the greatest interest has been in the positive muon due to the variety of possible sites for its location. The negative muon attaches itself to a nucleus and changes the charge of the host. The resulting nucleus probes the magnetic field at the nuclear site, which in many ways gives similar information to the Mossbauer or perturbed angular correlation techniques. Figure 5 shows the decay and frequency fits for μ^- in MnO. (3) MnO is an antiferro magnetic insulator. Note that the site of the muon can be selected by waiting until the μ^- Mn componant has disappeared due to μ^- nuclear capture.

On the other hand, the μ^+, being a positive impurity, occupies interstitial sites. It may migrate either by thermal excitation or phonon assisted tunneling or coherent cyclic orbiting. Therein lies both the advantage and disadvantage of the positive muon as a probe. The extent of our understanding of the precise site where the muon resides, the slowing down processes, thermalization, diffusion, radiative damage, defects, and trapping on impurities represents a challenge

to some and a monsterous obstacle to others. In some cases, the siting has been unambiguous. For example, the octahedral site in the single crystal of copper has been determined (4) by observing the variation of the damping or dipolar line broadening due to the copper host nuclear magnetic and electrostatic moments.

The motion of the μ^+ together with the action of random magnetic field fluctuations on the μ^+ spin, leads to a time dependence for the μ^+ asymmetry.

$$A(t) = \exp[2\sigma^2\tau^2(e^{-t/\tau} - 1 + t/\tau)], \tag{4}$$

where σ^2 is proportional to the second moment of the host nuclear dipole field $\langle M_2 \rangle$ and τ is the correlation time associated with the muon diffusion:

$$\frac{1}{\tau} = \frac{\langle v \rangle}{a} = \frac{D}{a^2} \text{ and } \sigma^2 = \frac{1}{2}\gamma_\mu^2[\langle M^2 \rangle = \langle \Delta B_{dip}^2 \rangle]. \tag{5}$$

(D is the diffusion coefficient, a is the lattice constant)

Figure 16 shows that at temperatures below 100°K the depolarization of the μ^+ appears to be consistent with the fields produced by the nuclear magnetic moments of the host copper nuclei. For short correlation times (fast hopping), $A(t) = \exp(-2\sigma^2\tau t)$, one has exponential decay with the damping rate $A = 2\sigma^2\tau$. For long correlation times, $A(t) = \exp(-\sigma^2 t^2)$, one has a Gaussian time dependence. In the actual situation the fits to either Gaussian or exponential are usually not sufficiently sensitive to differentiate

the two different forms. If one takes the characteristic time for 1/e reduction, then one has either $t_{relax} = A^{-1} = (2\alpha^2\tau)^{-1}$ or σ^{-1} in the two extremes.

The line broadening is proportional to the square of the dipolar field:

$$\Delta B^2_{dip} = \frac{1}{3}\gamma_s^2\hbar^2(S)(S+1)\sum_i (3\cos^2\theta_i - 1)^2 r_i^{-6}, \qquad (6)$$

By varying both the magnetic field and the crystal orientation as shown in Fig. 6, comparison with Table III clearly shows that the octahedral site is indicated as the muon site.

Indeed Teichler (5) has shown in Fig. 7 that the potential energy surface is lower in the O-site relative to the T-site.

Clawson, et al. (6) have used the ZF technique pioneered by the Tokyo group (7) in their work on spin glasses to explore the migration of μ^+ in cold copper. In Zero field the muon's initial polarization rotates in the random local fields and the componant along the initial direction washes out. To explain this technique Fig. 8 and Fig. 9 show the ZF relaxation function as a function of correlation time τ. MnSi at room temperature is essentially fixed, $\tau \to \infty$. Figure 10 shows the CERN data (8) for the relaxation vs temperature with Clawson's data (6) on high purity samples of copper obtained in transverse field measurements. Figure 11 and 12 show the longitudinal relaxation function (6). Note the surprising enhancement of the hopping rate of muons seems to occur as the temperature is lowered below 5K.

Here the μ spin for a muon at rest decays rapidly due to the coupling to the neighboring nuclear magnetic moments, goes to zero but after a while returns to approximately 1/3 of the initial polarization. Kubo and Toyabe (9) have shown that when there is hopping this approach to the asymptotic value is altered as shown in Fig. 9. For a time-independent Gaussian field distribution, the relaxation function is

$$G_z(t) = \cos^2\nu + \sin^2\nu \cos(\gamma_\mu H_d t)> = (1/3) + (2/3)(1-\Delta^2t^2)\exp(-1/2\Delta^2t^2), \quad (7)$$

where $\gamma_\mu = 2\pi \times 13.55$ kHz/Oe is the μ^+ gyromagnetic ratio, Δ/γ_μ is the width of a single component of $\vec{H}_d$, and ν is the angle between $\vec{H}_d$ and the muon spin. This function initially decays as $\exp(-\Delta^2t^2)$, reaches a minimum at $t_{min} = \sqrt{3}\Delta^{-1}$, and recovers to 1/3 as $t \to \infty$.

Figures 13, 14, and 15 are the results of a recent calculation by Holzschuh and Meier (10) which is a dynamical calculation using the shells of nearest neighbors in which the hopping frequency is varied. This result can be compared to the data in Fig. 10, again indicating an increased hopping at low temperature.

At elevated temperatures the thermal activated diffusion is observed in metals. Figure 16 and 17 show the Arrhenius behavior and Table 4 gives the activation energy and attempt frequency for a few of the metals.

If we characterize the data with classical Arrhenius description for the transition rate, we find $W = \tau^{-1} = Da^{-2} = \nu_o\exp(-QkT)$, where τ is the time between collisions, D is the diffusion coefficient, a is the lattice constant, ν_o is the "preexponential" attempt frequency, and Q is the height of the barrier or activation energy.

In the small polaron model of diffusion, phonons activate the motion of muons over the barrier. At low temperature (<5k), very slow hopping occurs. Is this some type of quantum tunneling?

The theorists models (11) do not agree entirely and there is still much to be learned, for example, by introducing dilute magnetic impurities. Experiments underway are aimed at this important problem.

Some of the most recent new developments in μSR are related to the muonium formation in insulators. For many years muonium precession in solids was not seen at all. With recent strong field techniques the rapid depolarization due to local fields can be decoupled. Figure 18 shows the hyperfine splitting of the muonium energy leveles vs magnetic field. The interaction is

$$H^{Mu} = \frac{\hbar}{4}\omega_o(\sigma^\mu \cdot \sigma^e) + \frac{\hbar}{2}\omega^\mu \cdot \sigma^\mu + \frac{\hbar}{2}\omega^e \cdot \sigma^e \qquad (8)$$

By choosing a magic field where the ν_{12} and ν_{34} are independent of external field, Kiefl et al (12) have recently obtained many of the muonium huperfine splitting frequencies to better than a tenth percent accuracy. Figure 19 shows the fourier transform of the time distribution for quartz. $\nu_o = \nu_{12} = \nu_{34}$.

This results in a picture where in most insulations muonium is formed in abundance. Quantitative work in the interpretation of these frequencies promises to be particularly exciting.

Muonium in semiconductors has also seen some very important advances. Figure 20 shows the original fourier spectrum of silicon compared to quartz. Note the extra anomalous lines and the change in the separation of the two higher frequencies. Figure 21 shows the early

magnetic field variation of frequency data. For anomalous muonium

$$H^* = h\nu\, \vec{S}_\mu \cdot \vec{S}_e + h\delta\, S_\mu{}^z S_e{}^z + g_e\mu_B\, \vec{S}_e \cdot \vec{B} + g_\mu\mu_\mu\, \vec{S}_\mu \cdot \vec{B}$$

therefore

$$\nu_{21} = \left[(\gamma_\mu B + \tfrac{1}{2}(\nu + \delta\, \cos^2\Theta))^2 + \frac{\delta^2}{4}\, \sin^2\Theta\cos^2\Theta\right]^{1/2}$$

$$\nu_{34} = \left[(\gamma_\mu B - \tfrac{1}{2}(\nu + \delta\, \cos^2\Theta))^2 + \frac{\delta^2}{4}\, \sin^2\Theta\cos^2\Theta\right]^{1/2}. \qquad (9)$$

Figure 22 includes the newer high field data which pins down the additional interaction Hamiltonian which was found to be $\alpha\, S_\mu^t\, S_e^z$ with the z axis along the 111 axis. By improved timing techniques Holzschuh (12) has observed the direct hyperfine transition in silicon and Germanium. See table 5.

Recently Patterson has used channeling to try to pin down the location of the muon in the decay of muons in silicon. Figure 23 shows the shadows of the 110 plane in the decay electron distribution arising from the Mu^* state. He concludes (tenatively) that the Mu^* lies on a [111] atomic string "concentrated in two small regions on either side of the T site one toward but not including the AB site and one toward out not including the H site." (12)

Ferromagnetic, antiferromagnetic superconducting and other exotic materials have been the focus of a number of studies. As the muon is a clock proportional to the local magnetic field at its location in the crystal lattice it will indicate the phase transitions in a dramatic fusion. Figure 24 shows the rapid oscillation of the μ spin in pure iron in zero applied field. Given a local dipolar field of about $\pm$10KG these data imply a μ^+ hopping rate >10" sec^{-1} even at room temperature. Figures 25, 26, 27, and 28 show the behavior in cobalt

with no applied field, (15) as the frequency shifts rapidly as a function of temperatures. The hyperfine field measurements and calculation of their magnitudes is another challenging story which is still unfolding. The inhomogeneities in the neighborhood of the probe near phase transitions gives a relaxation or broadening of the line which is potentially a measure of the coherence length for the fluctuating magnetic field.

These calculations together with the Knight shifts have shown that the usual Jellium model for electrons in metals must be radically modified to realistically match the data, a result which came as a surprise to some, and to others, a challenge.

The critical behavior in various ferromagnetic and antiferromagnetic insulators as well as those which undergo superconducting transitions has attracted other groups.

Certainly the variety of interesting possibilities is no limit for hunting. However, it must be noted that in many cases the muon is still an infant and to quality as a serious probe of magnetic materials, many questions must be answered.

This review must close with a disclaimer concerning the completeness of the subject. I have sampled arbitrarily just a small fraction of the work going on today as I mentioned at the outset. I hope to have given you a flavor of the subject, seen from a personal viewpoint of an experimentor at close distance.

This work was supported in part by the U.S. Department of Energy under Contracts DE-AC03-76SF00098, W-7405-ENG-36, and AT03-81ER40004.

BIBLIOGRAPHY

1. Brewer, J.H., Crowe, K.M., Gygax, F.N., Schenck, A. Muon Physics, Vol. III, (ed. V.W. Hughes, C.S. Wu) pp. 3-139. New York: Academic Press (1975); Brewer, J.H., Crowe, K.M., Advances in Muon Spin Rotation, Ann. Rev. Nucl. Part. Sci. 28, p. 239 (1978); Schenck, A. On the Applications of Polarized Positive Muons in Solid State Physics. Nuclear and Particle Physics at Intermediate Energy, ed. J.B. Warren. New York:Plenum Press (1976); Seeger, A., Hydrogen in Metals I (G. Alefeld & J. Volkl, Springer Verlag) (1978); Karlsson, E., Phys. Rep. 82, 271 (1982); Heffner, R., Proceedings of the Workshop on Muon Science and Facilities at Los Alamos, p.76, see LA-9582-C (March 15, 1982); Gygax, F.N., Kundig, W.K., Meier, P.F., Hyperfine Interactions 6, (1978); Brewer, J.H., and Percival, P.W., Hyperfine Interactions 8, p. 831 (1981).

2. Pifer, A.E., Bower, T., Kendall, K.R. Nucl. Instrum. Methods 135, p. 39 (1976).

3. Nagamiya, S., Nagamine, K., Hashimoto, O., Yamazaki, T. Physical Rev. Lett. 35, p. 308 (1975).

4. Camani, M., Gygax, F.N., Ruegg, W., Schenck, A., Schilling, H. Phys. Rev. Lett. 39, p. 836 (1977).

5. Teichler, H., Exotic Atoms '79, Fundamental Interactions and Structure of Matter, ed. Kenneth Crowe, p. 296, New York:Plenum Press, (1980).

6. Clawson, W.W., et al., Phys. Rev. Lett. 51, p. 114 and references therein (1983).

7. Hayano, R.S., et al., Phys. Rev. B 20, p. 850 (1979).

8. Hartmann, O., et al., Phys. Rev. Lett. 44, p. 337 (1980).

9. R. Kubo and T. Toyabe, in Magnetic Resonance and Relaxation, ed. by R. Blinc, p. 810 (North-Holland, Amsterdam, 1967); T. Toyabe, M.S. Thesis (University of Tokyo 1966) unpublished.

10. Holzschuh and Meier, private communications.

11. A.M. Stoneham, Yamada Conference on μSR, Shimoda Japan conference proceeding in press (April 1983). See other papers included therein.

12. E. Holzschuh, R. Kiefel, W. Kundig. W. Odermatt, B.D. Patterson, Wissenschaftlicher Jahre Bericht, Univ. at Zruich, p. 46 (1982/83).

13. Patterson, B.D. Hintermann, A., Kundig, W., Meier, P.F., Waldner, F., Graf, H., Rechnagel, E., Weidinger, A., Wichert, Th., Phys. Rev. Lett. 40, p. 1347 (1978).

14. T. Yamasaki, Hyperine Interactions 6, p. 115 (1979).

15. Graf, H., Kundig., W., Patterson, B.D., Reichart, W., Roggwiller, P., Camani, M., Gygax, F.N., Ruegg, W., Schenck, A., Schilling, H., Meier, P.F. Phys. Rev. Lett. 37, p. 1644 (1976); Nishida, N., Nagamine, D., Hayano, R.S., Yamazaki, T., Fleming, D.G., Duncan, R.A., Brewer, J.H., Ahtar, A., Yasuoka, H. Jpsn. J. Phys. Soc. (1978).

FIGURE CAPTIONS

Fig. 1 No caption

Fig. 2 μ^+-decay spectrum: isotropic contribution for the energy spectrum of the decay positron C (upper curve), and energy dependence of the asymmetry factor D, assuming $\xi = 1$ (lower curve).

Fig. 3 Angular relations between detector axis, spin orientation of the stopped μ^+, and a coplanar positron emission direction.

Fig. 4 Schematic plan view of the spectrometer and low temperature refrigerator.

Fig. 5 (Upper) μ^-SR time spectrum in MnO, showing the different lifetimes for μ^- bound to Mn and O. (Lower) μ^-SR frequency spectra in C and MnO at 6.9 kG showing a shift in the frequency of μ^-O relative to μ^-C. See reference (3).

Fig. 6 The field variation of the measured damping constant σ for μ^+ in a single crystal of copper oriented with the external field B_{ext} along different crystal axes. Assuming an interstitial octahedral site for the μ^+ the dashed curve was calculated including the quadrupole electric field gradient energy shift with no lattice distortion. The solid curve assumes a 5% dilation of the nearest neighbor separation. The pure magnetic splitting (Van Vleck values) are shown on the right.

Fig. 7 Potential energy of positive point charges in Cu calculated in the rigid lattice approximation and ground-site levels for μ^+ and p at O sites.

Fig. 8 Observed μ^+ longitudinal relaxation functions in MnSi at room temperature with 0, 10, and 30 Oe external fields. The solid curves are the best fits. See reference (7).

Fig. 9 (a) Zero-field longitudinal relaxation functions for different correlation times, numerically calculated.

(b) High-field transverse relaxation function plotted for different values of τ for comparison. See references (7), (9).

Fig. 10 Second moment of the Gaussian width of the muon depolarization rate in transverse field. The second moment is defined in the same way. The Gaussian width parameters are formally related as $\sigma = \Delta/\sqrt{2}$.

Data of ref. (8):
- □ polycrystalline copper, 520 Oe.
- ○ polycrystalline aluminum, 120 Oe.
- ● Polycrystalline aluminum, 520 Oe.

Data of ref. (6):
- ▲ oxygen annealed high purity copper single crystal 80 Oe.
- △ same copper target material as above, (8) 80 Oe.
- ⊗ high purity aluminum polycrystal, 80 Oe.

Fig. 11 Experimental data for $G_z(t)$ at three representative temperatures. The lines are the theory of Ref. (7) fitted to the data.

Fig. 12 Temperature dependence of (a) zero-field dipolar width and (b) hopping rate and diffusivity. The lines are drawn only to guide the eye.

Fig. 13 Comparison of the Kubo-Toyabe function (dashed line) with the polarization of a muon at the octahedral site in a fcc-lattice interacting with J=3/2 nuclei on the first and second neighbor shells. Time in units of $1/\omega_1$. Parameter Δ has been chosen such that both curves have the same second moment M = 24 + 80/81. See Fig. 4.

Fig. 14 Polarization for a muon interacting with N = 4, 6, or 8 nuclei with J=3/2 in a tetrahedral (T), octahedral (O), or cubic (C) arrangement, respectively. Time in units of $1/\omega^{Decay}$. See Fig. 1.

Fig. 15 Dynamic polarization functions obtained from the solution of the integral equation for hopping rates ν = 0.2, 0.5, 1, or 2 x ω_1 as indicated. The curve ν = 0 is the static function. Time in units of $1/\omega_1$. See Fig. 5.

Fig. 16 The temperature variation of the μ^+ depolarization rate for vanadium, copper, gallium, antimony, and indium. A(T) was obtained using a Gaussian fit for the asymmetry time variation $A(t) = \exp(-A^2t^2)$.

Fig. 17 A summary of the Arrhenius plots for the hopping rate, inversely proportional to the correlation time τ vs reciprocal temperature.

Fig. 18 Energy eigenstates of 1 = 0 muonium in an external magnetic field, as a function of the dimensionless "specific field".

$$\chi = 2\omega_+/\omega_0 = (g_e\mu_0{}^e - g_\mu\mu_0{}^\mu)|B|/(\hbar\omega_0) = \frac{B}{1585}$$

For graphical clarity, an unphysical value of $|\mu_0{}^e/\mu_0{}^\mu|$ is used to generate the plot. The four allowed transitions ($\Delta m = \pm 1$) are indicated.

Fig. 19 μSR frequencies measured at the "magic" field in quartz. The line at 154.8 MHz is form μ^+ and the lines ν_{12} and ν_{34} correspond to muonium.

$$\nu_0 = \nu_{12} + \nu_{34} = 4496 \text{ MHz}.$$

Fig. 20 Frequency spectra (square of the Fourier amplitudes, arbitrary units) of muons in fused quartz at room temperature and in p-type silicon at 77°K. In both cases the applied transverse field is 100 G. The prominenet peaks (from left to right) are: the free muon precession signal at 1.36 MHz; a characteristic background signal at 10.2 MHz, due to rf structure in the cyclotron beam; the two anomalous frequencies at 43.6 $\pm$ 2.9 MHz (silicon only); and the two 1s muonium peaks centered about 139 MHz. The wider splitting of the two 1s muonium lines in silicon is due to the weaker hyperfine coupling (from Brewer et al., 1973a).

Fig. 21 Dependence of anomalous frequencies in silicon on field strength and crystal orientation. Round points and solid lines are data and best fir for [111] crystal axis along the field; triangular points and dashed lines are data and best fits for [100] axis along the field. Free muon, 1s muonium, and cyclotron background signals are not shown. A number of peaks appear in the spectra in addition to the fitted "proper anomalous frequencies; these are unexplained. They are indicated by square points (for prominent peaks) and horizontal bars (for weak or questionable peaks). The higher of the "proper" anomalous frequencies is missing at several fields.

This is because the spectra showed no statistically significant peaks at those positions.

Fig. 22 Experimentally observed precession frequencies in Si as a function of the external field. Theoretical curves are included for the μ^+ components (solid line) and for the Mu^* components.

Fig. 23 (a) A $\mu^+ \rightarrow e^+$ channelling pattern for a [111] Si crystal at room temperature. Comparison with a Laue X-ray exposure of the sample, shown in (b) identifies the lines of minimum counting rate as a (110) planar blocking effect. The reduced rate at the center of the pattern is a [111] axial dip.

Fig. 24 Forward/backward asymmetry for μ^+ in Fe single crystal.

Fig. 25 Time spectrum of a μSR experiment in Co at zero applied field[4].

Fig. 26 The two muon interstitial sites in the hep crystal structure of cobalt.

Fig. 27 Observed precession frequencies in Co as a function of temperature.

Fig. 28 The temperature dependence of the measured local field B_μ and the various contributions to B_μ. The Lorentz field B_L and the dipolar field B_{dip} were calculated as described in the text. The figure shows the projection of $\vec{B}_{dip}$ along the local magnetization direction. The hyperfine field B_{hf} was then computed from the measured values. The solid and dashed curves for B_{dip} and B_{hf} refer, respectively, to the octahedral and tetrahedral interstitital site assignments. The easy axis of magnetization changes in the temperature range 500 to 600 K.

A phase change from hop to fcc occurs at 690 K. The sign B_μ is defined with respect to the local magnetization direction.

GASES:

Atomic Physics:

- Charge-Changing Collisions of μ^+ -- $\mu^+ \rightleftarrows$ Mu and muonium formatio in noble gases.

Muonium Chemistry:

- Thermal Reacion Kinetics of Mu, H -- quantum tunneling

LIQUIDS:

Radiation Chemistry:

- Muonium Hot Atom Reactions
- Spur Reactions
- Muonic Radicals

Muonium Chemistry:

- Thermal Reaction Kinetics of Mu, H -- comparison with gases

METALS:

Interstitial Magnetism via μ^+SR:

- Dipolar Fields and μ^+ Sites
- Spin-dependent Screeming -- hyperfine fields, Knight shifts
- Critical Phenomena -- fluctuations, phase transitions

Magnetism as Lattice Sites via μ^-SR

Hyperfine Field Gradients

μ^+ Spin Relaxation and Motion of Light Interstitials:

- Quantum Diffusion
- Defect Trapping
- Impurity Trapping

NONMETALS

Magnetism in Insulators via μ^+SR:

- Local Fields and Shifts
- Relaxation and Spin Fluctations
- Phase Transitions
- Spin glasses

Muonium in Nonmagnetic Insulators:

- Mu Formation and Relaxation
- Mu Diffusion
- Mu in Powders -- ejection into vacuum, surface physics

μ^+ and Mu in Semiconductors:

- μ^+SR Spectroscopy -- structure of μ^+e bound states

Fig. 1

TABLE 1

Muon Properties

Spin	$1/2$
Mass	$m_\mu = 105.6595(3)$ MeV $= 206.76826(6) m_e$ $= 0.1126123(6) m_p$
Magnetic moment	$\mu_\mu = \lvert g_\mu S_z \rvert \frac{e\hbar}{2m_\mu c} = 3.183345(9)\mu_p$ $= 28.0272(2) \times 10^{-18}$ MeV/G
Bohr radius	$a_B \mu = \frac{\hbar^2}{m_\mu e^2} = 255.927$ fm $= 2.55927 \times 10^{-11}$ cm
Compton wavelength	$\chi_\mu = \frac{\hbar}{m_\mu c} = 1.86758$ fm
Lifetime	$\tau_\mu = 2.1994(6) \times 10^{-6}$ sec
Muonium Hyperfine frequency	$\nu_o = 4463.30288(16)$ MHZ

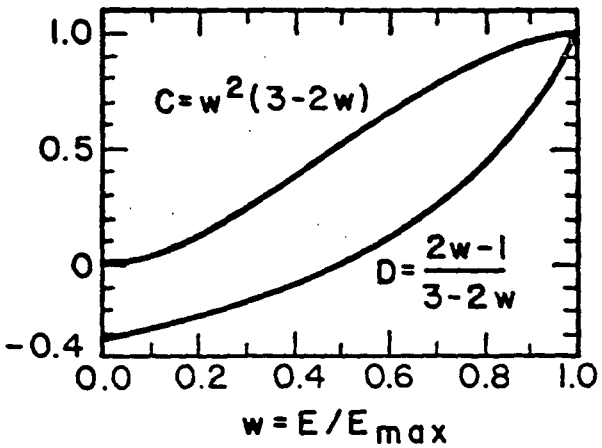

Fig. 2

Table 2. Observable muon and muonium precession frequencies and the corresponding cycle periods for a magnetic field strength B

B (kG)	0.1	0.1	1	10	100
$\lvert\nu^{\mu}\rvert$ (MHZ)		1.355	13.55	135.5	1355
$T_{\mu} = 1/\lvert\nu^{\mu}\rvert$ (nsec)		740	74	7.4	0.74
$\lvert n^{Mu}\rvert$ (MHz)	13.94	139.4	1394		
$T_{Mu} = 1/\lvert\nu^{Mu}\rvert$ (nsec)	72	7.2	0.72		

Table 3. Damping rate (μsec^{-1}) due to nearest neighbor Cu nuclei

	External field parallel to		
Site	(100)axis	(110)axis	(111)axis
Octahedral	0.308	0.165	0.0674
Tetrahedral	0.0771	0.279	0.319

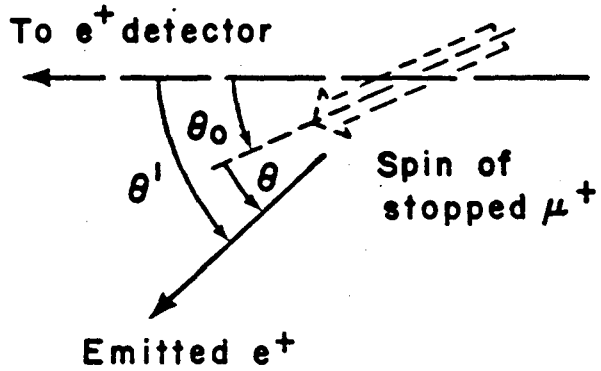
To e^+ detector
θ_0
θ'
θ
Spin of stopped μ^+
Emitted e^+

Fig. 3

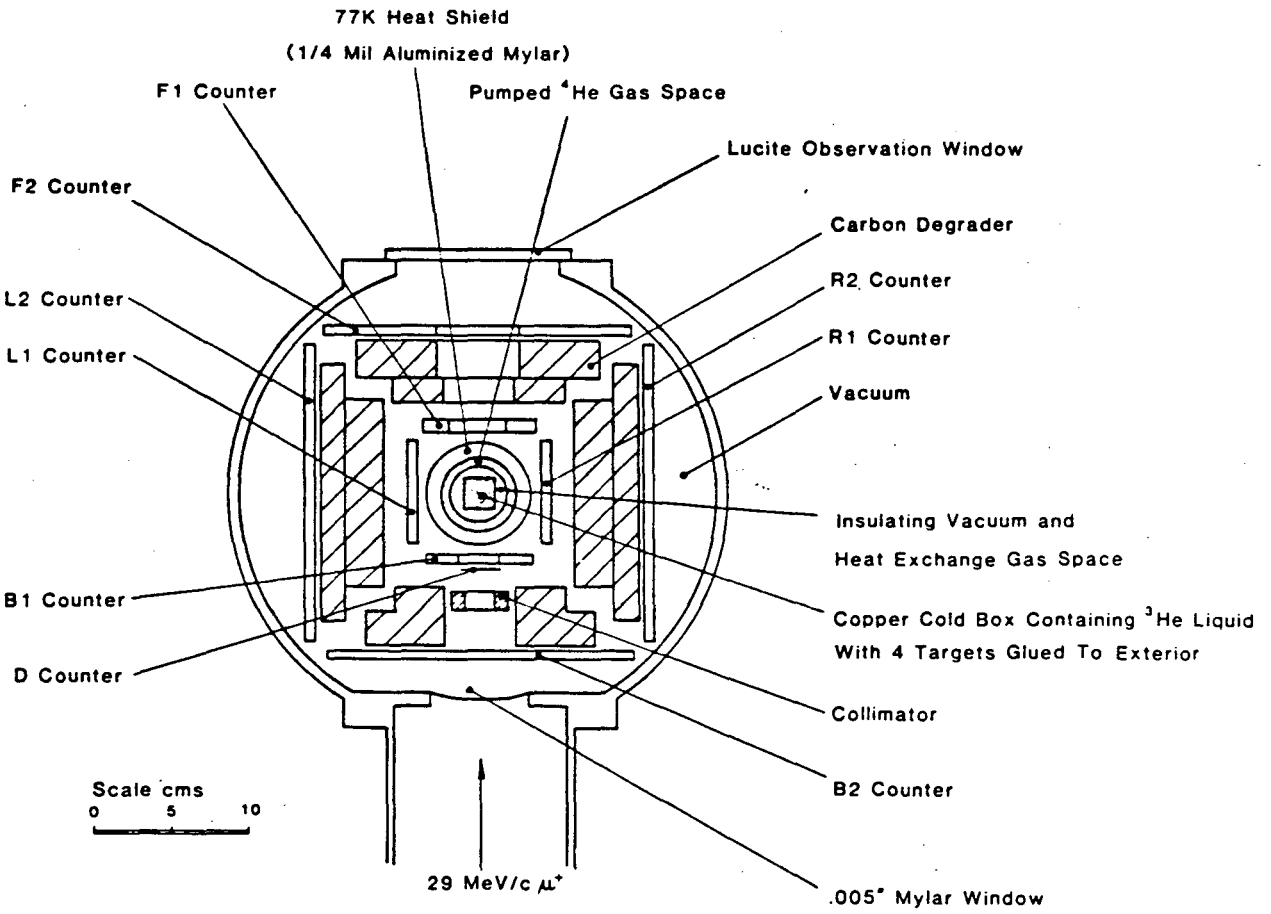
77K Heat Shield
(1/4 Mil Aluminized Mylar)
F1 Counter
Pumped ^{4}He Gas Space
Lucite Observation Window
F2 Counter
Carbon Degrader
L2 Counter
R2 Counter
L1 Counter
R1 Counter
Vacuum
Insulating Vacuum and
Heat Exchange Gas Space
B1 Counter
Copper Cold Box Containing ^{3}He Liquid
With 4 Targets Glued To Exterior
D Counter
Collimator
B2 Counter
Scale cms
0 5 10
29 MeV/c μ^+
.005" Mylar Window

Fig. 4

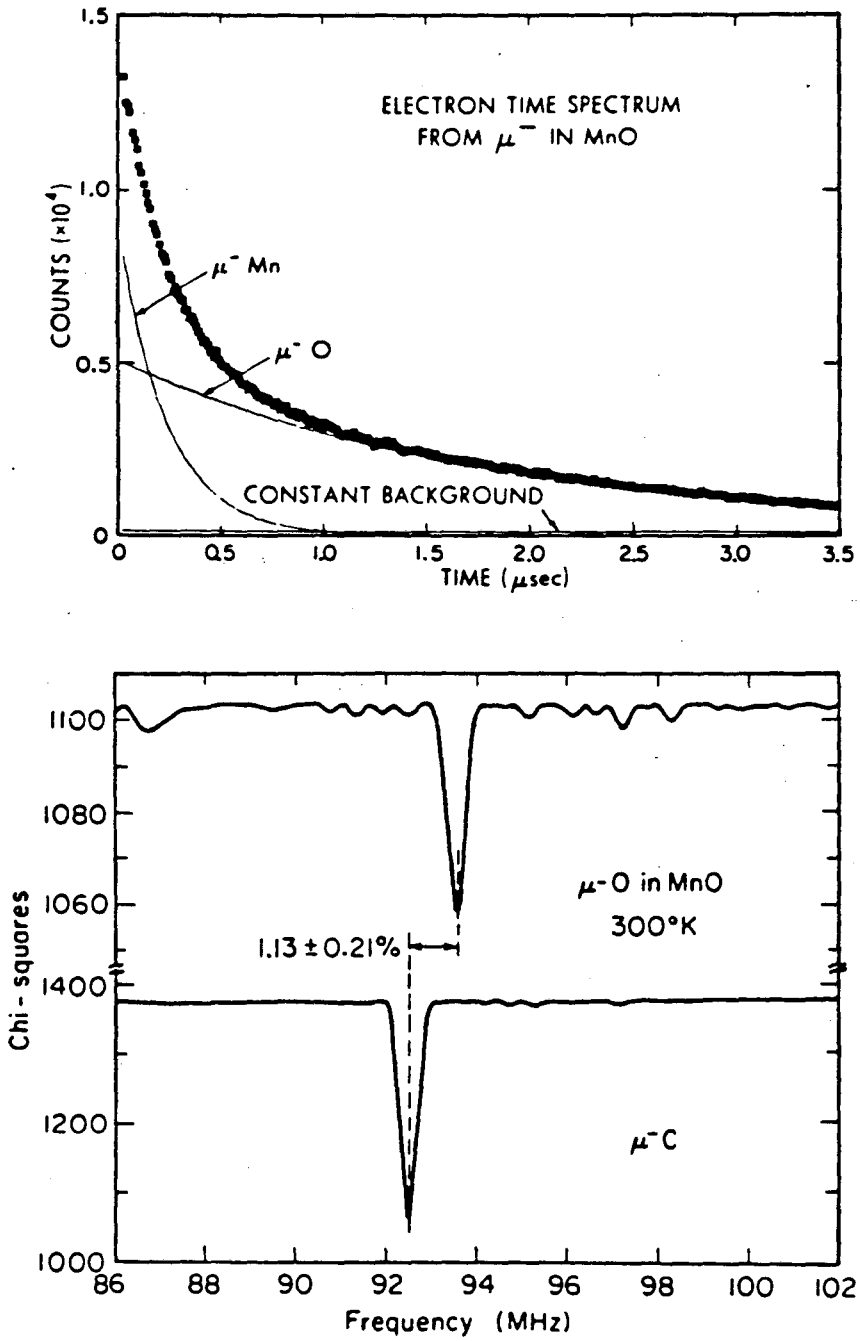
ELECTRON TIME SPECTRUM
FROM μ⁻ IN MnO
COUNTS (×10⁴)
μ⁻ Mn
μ⁻ O
CONSTANT BACKGROUND
TIME (μsec)
μ-O in MnO
300°K
1.13 ± 0.21%
μ⁻C
Chi - squares
Frequency (MHz)

Fig. 5

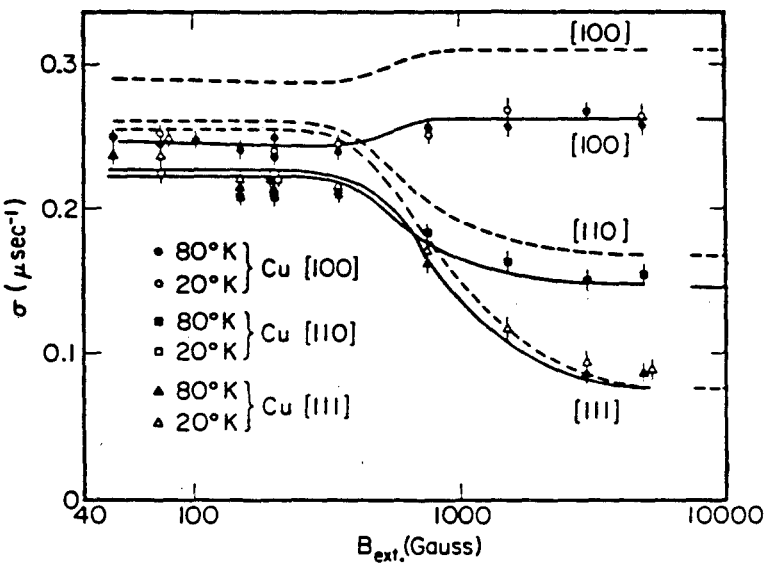
[100]
[100]
[110]
[111]
0.3
0.2
0.1
0
σ (μsec⁻¹)
• 80°K
○ 20°K
Cu [100]
■ 80°K
□ 20°K
Cu [110]
▲ 80°K
△ 20°K
Cu [111]
40
100
1000
10000
B_ext.(Gauss)

Fig. 6

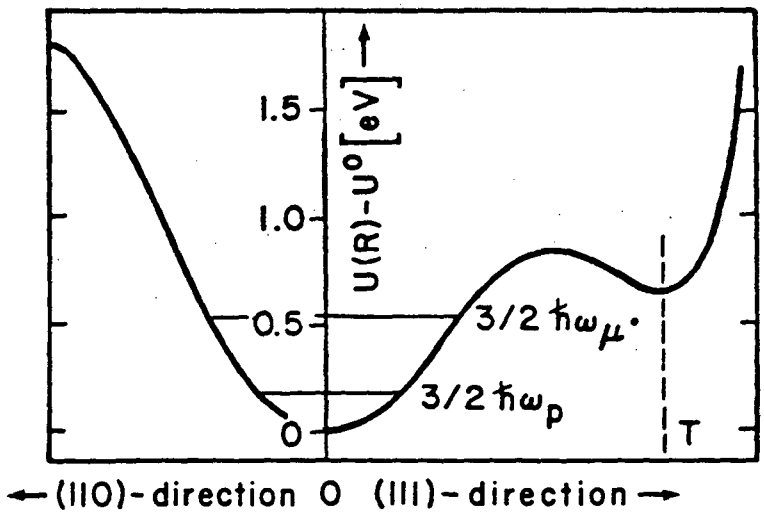

Fig. 7

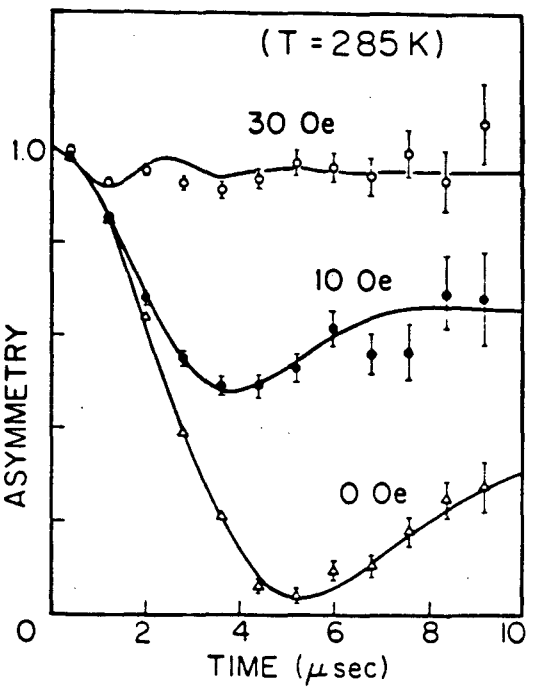

Fig. 8

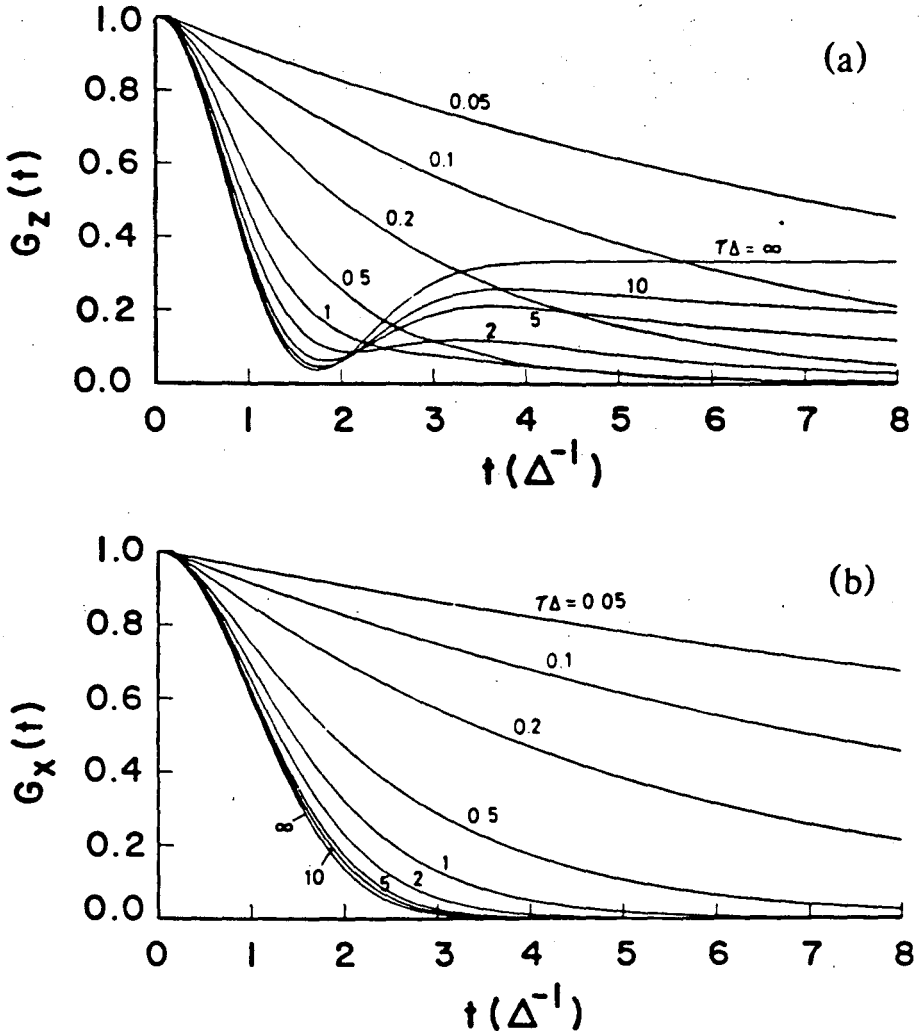
(a)
$G_z(t)$
1.0
0.8
0.6
0.4
0.2
0.0
0.05
0.1
0.2
0.5
1
2
5
10
$T\Delta = \infty$
0 1 2 3 4 5 6 7 8
$t(\Delta^{-1})$
(b)
$G_x(t)$
$T\Delta = 0.05$
0.1
0.2
0.5
1
2
5
10
8
0 1 2 3 4 5 6 7 8
$t(\Delta^{-1})$

Fig. 9

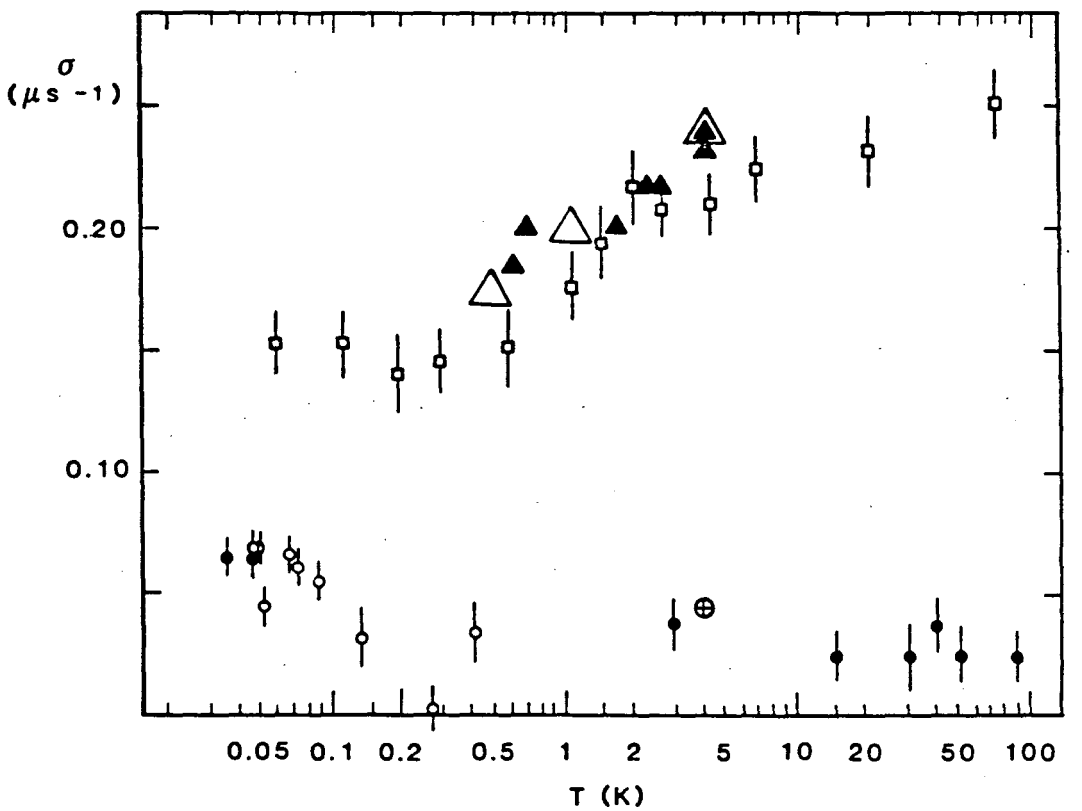

Fig. 10

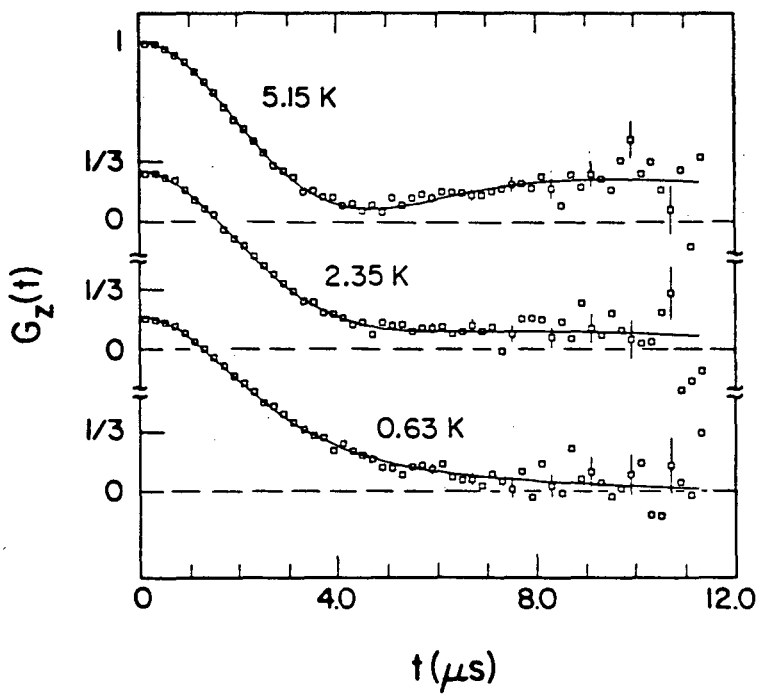

Fig. 11

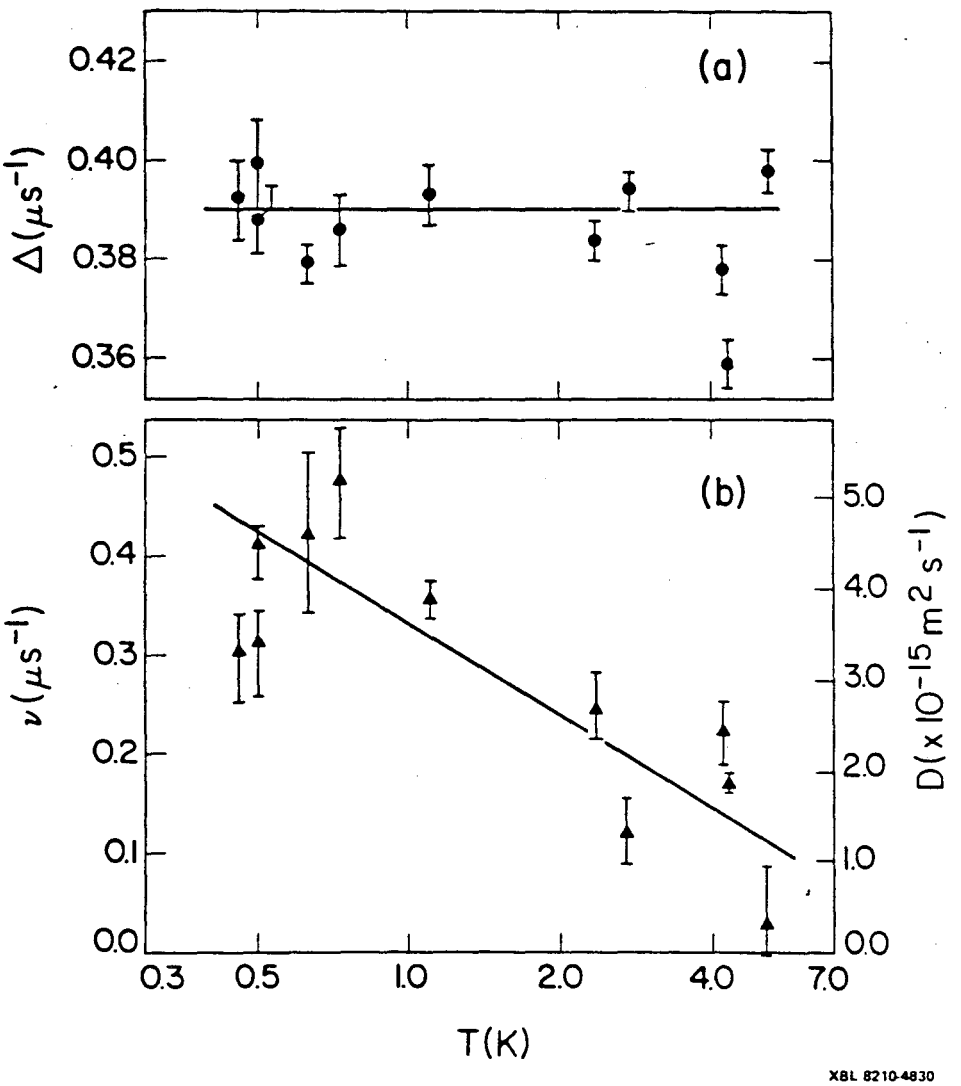
(a)
0.42
0.40
0.38
0.36
Δ(μs⁻¹)
(b)
0.5
0.4
0.3
0.2
0.1
0.0
ν(μs⁻¹)
5.0
4.0
3.0
2.0
1.0
0.0
D(x 10⁻¹⁵ m² s⁻¹)
0.3
0.5
1.0
2.0
4.0
7.0
T(K)
XBL 8210-4830

Fig. 12

Fig. 13

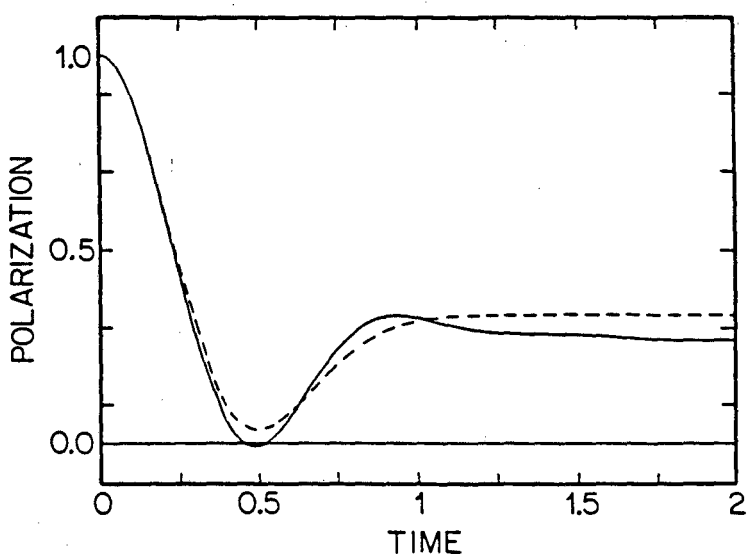

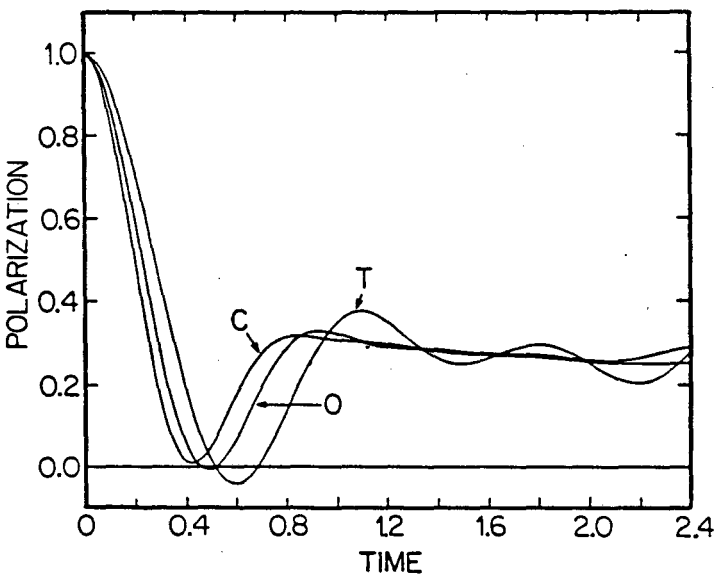

Fig. 14

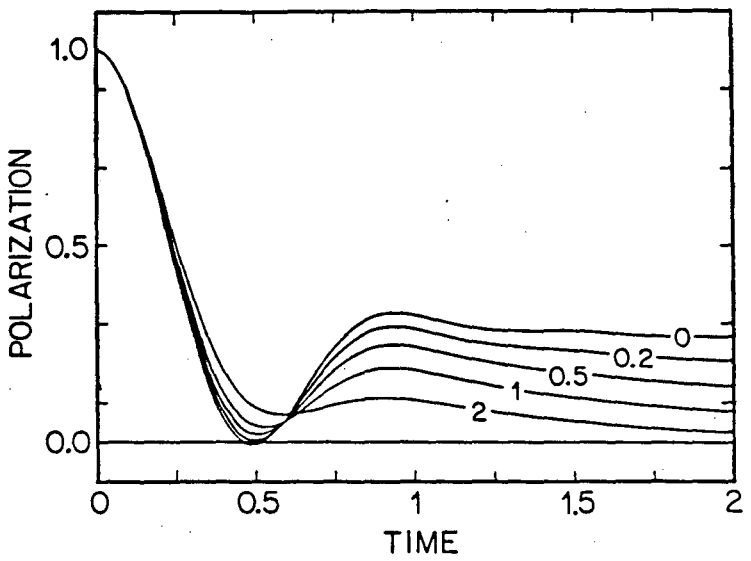

Fig. 15

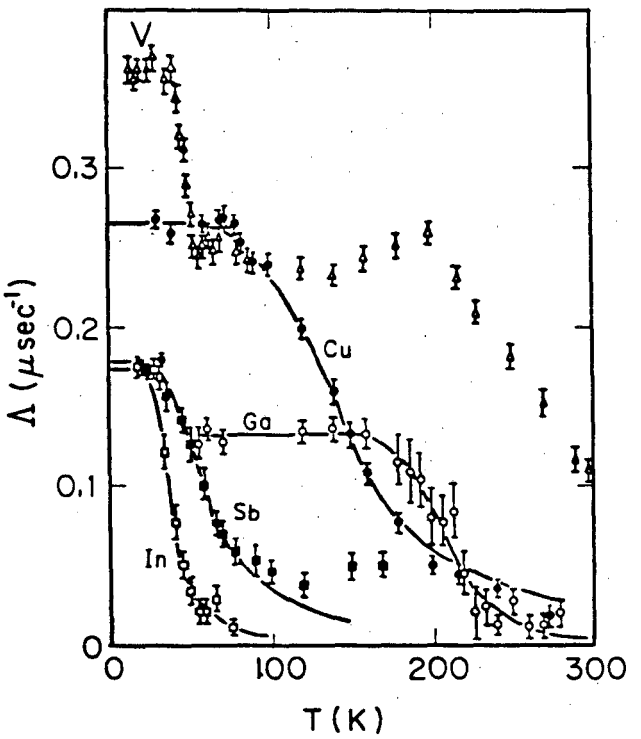

Fig. 16

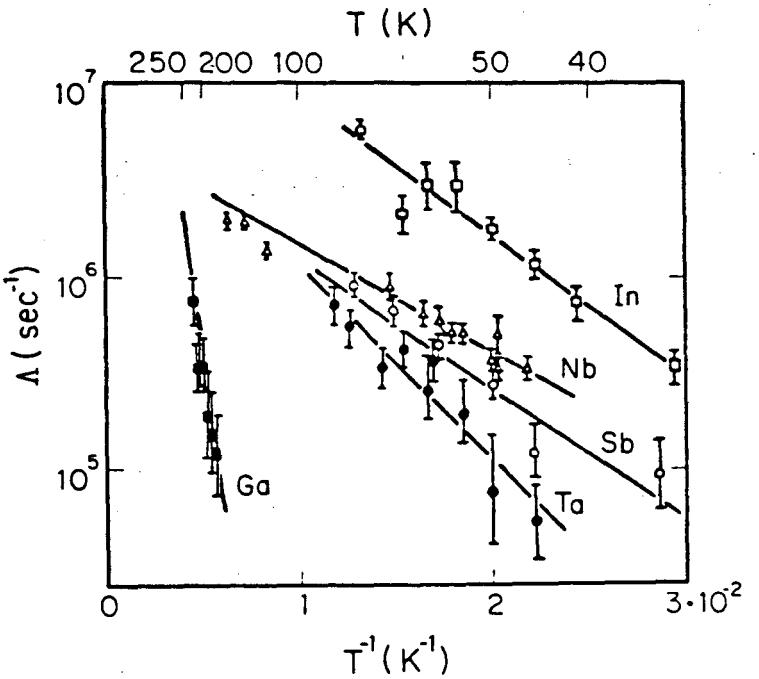

Fig. 17

Table 4 The preexponential attempt frequency ν_0 and the activation energy Q obtained from the muon relaxation rates

Element	$\log_{10} \nu$	Q/k (K)	Q (10^{-3} ev)
Cu	7.61 ± 0.04	560	48.2
Sb	6.97 ± 0.14	173	14.9
Be	9.5 ± 0.4	1200	103.4
In	6.7 ± 0.2	155	13.3
Ta	6.9 ± 0.2	200	17.2
Ga	10.1 ± 0.8	2130	183.5
Nb	6.5	100	8.61
Bi	11.2	1400	120.6

Table 5 Spin Hamiltonian and Hperfine Parameters of Normal and Anomalous Muonium.

Normal Muonium

$$\mathcal{H} = g\mu_B \bar{H} \cdot \bar{S} + A\bar{S} \cdot \bar{I} - g_\mu \mu_\mu \bar{H} \cdot \bar{I} \qquad \text{(isotropic)}$$

A = 4463.30288(16) MHz	in vacuum
A = 3700(50) MHz	in diamond
A = 2011.8(5) MHz	in Silicon
A = 2361(3) MHz	in germanium

Anomalous Muonium

$$\mathcal{H} = g_{\|} \mu_B H_z S_z + g_\perp \mu_B (H_x S_x + H_y S_y) + A_{\|} S_z I_z$$

$$+ A_\perp (S_x I_x + S_y I_y) - g_\mu \mu_\mu \bar{H} \cdot \bar{I} \qquad (z \| \langle 111 \rangle)$$

$A_{\|}$ = -167.9(1)MHz $A_\perp$ = 392.4(1)MHz	(in diamond, T = 4 K)
$A_{\|}$ = 16.790(11)MHz $A_\perp$ = 92.588(50)MHz	(in silicon, T OK)
$A_{\|}$ = 26.8(10)MHz $A_\perp$ + 130.7(10)MHz	(in germanium, T = 10 K)

The values of $g_{\|}$ and $g_\perp$ are not known accurately (but they are near 2.0).

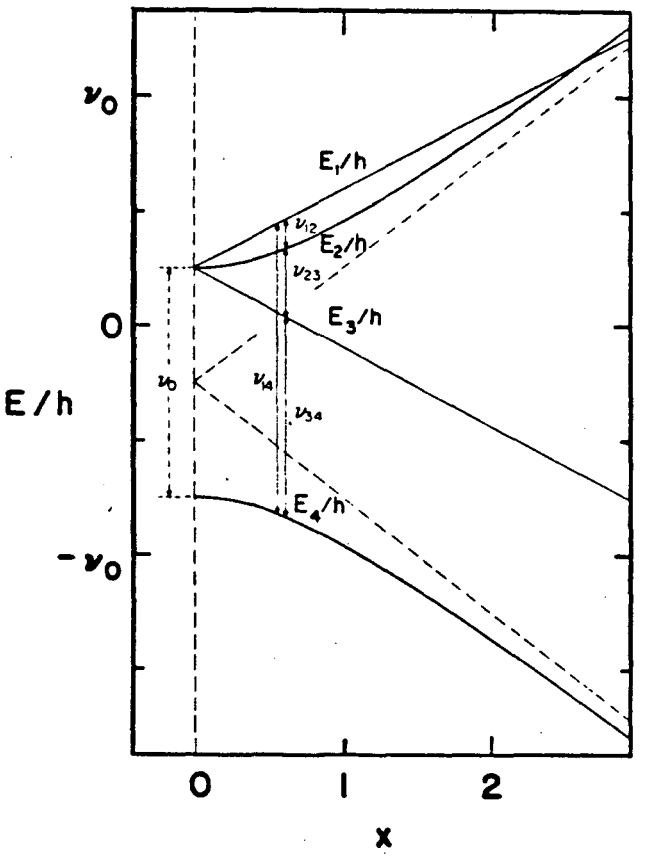
ν_0
0
$-\nu_0$
E/h
E_1/h
E_2/h
E_3/h
E_4/h
ν_{12}
ν_{23}
ν_{14}
ν_{34}
ν_0
0
1
2
x

Fig. 18

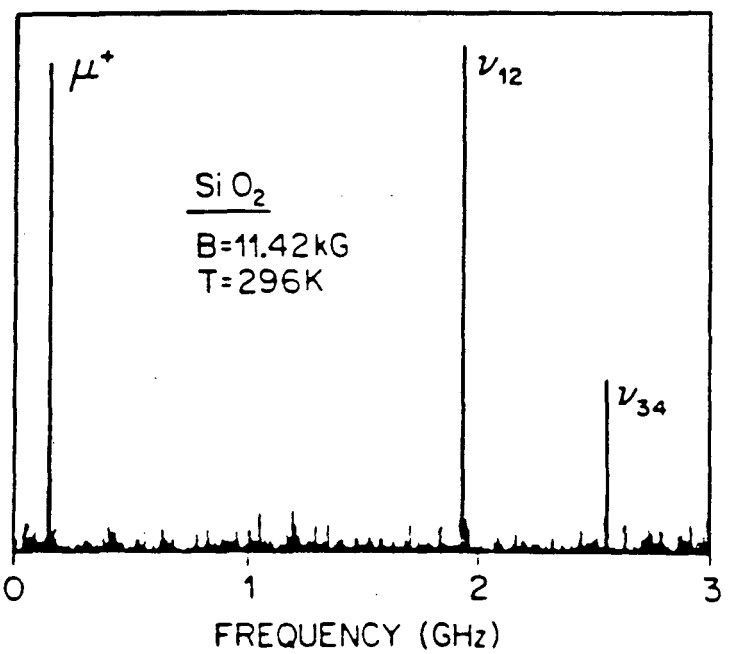
μ^+
ν_{12}
ν_{34}
SiO_2
B=11.42kG
T=296K
0
1
2
3
FREQUENCY (GHz)

Fig. 19

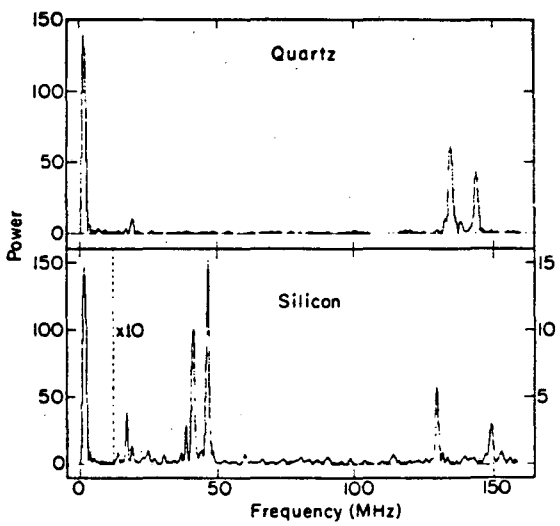

Fig. 20

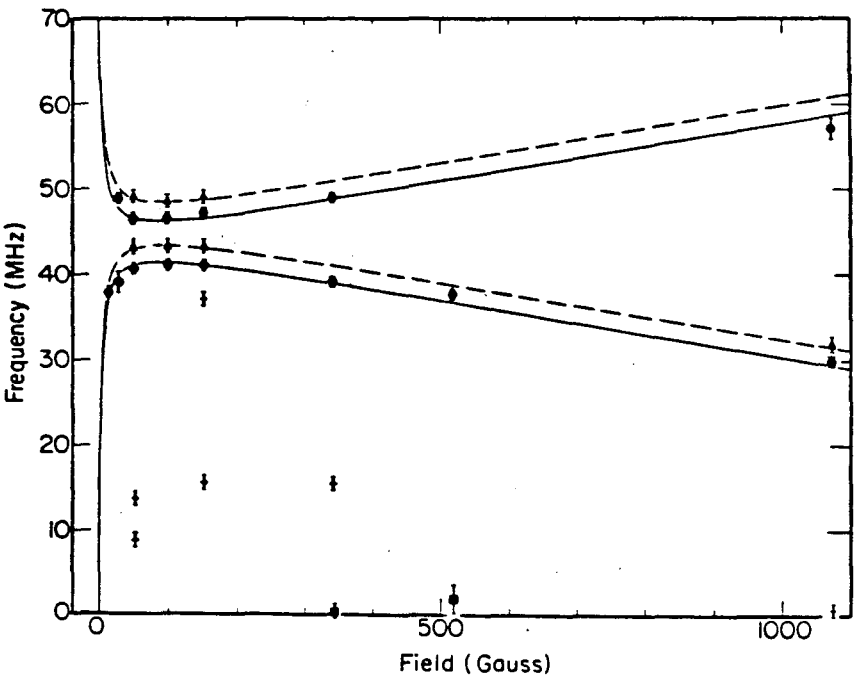

Fig. 21

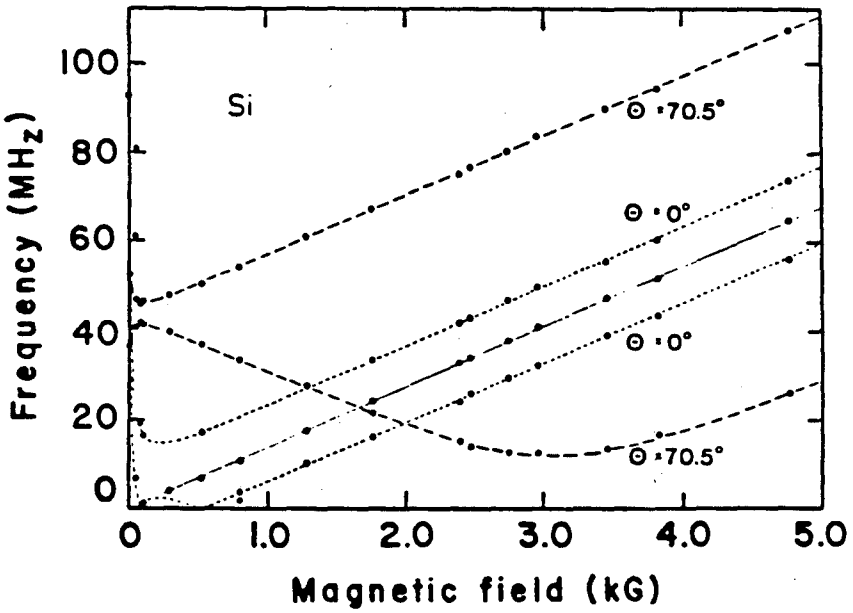
Si
Θ = 70.5°
Θ = 0°
Θ = 0°
Θ = 70.5°
Frequency (MHz)
Magnetic field (kG)
0
20
40
60
80
100
0
1.0
2.0
3.0
4.0
5.0

Fig. 22

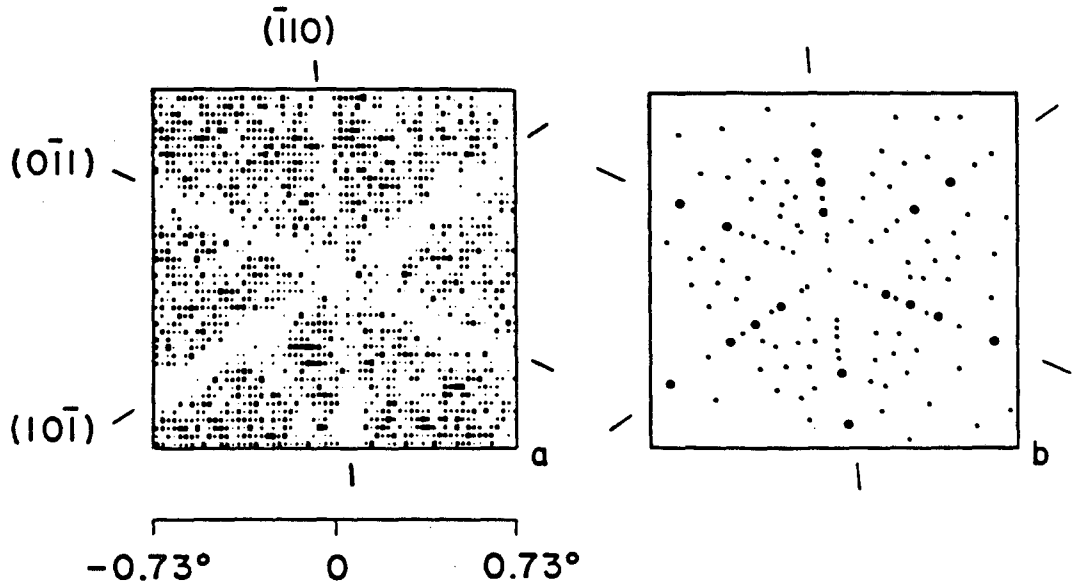
(1̄10)
(01̄1)
(101̄)
a
b
-0.73°
0
0.73°

Fig. 23

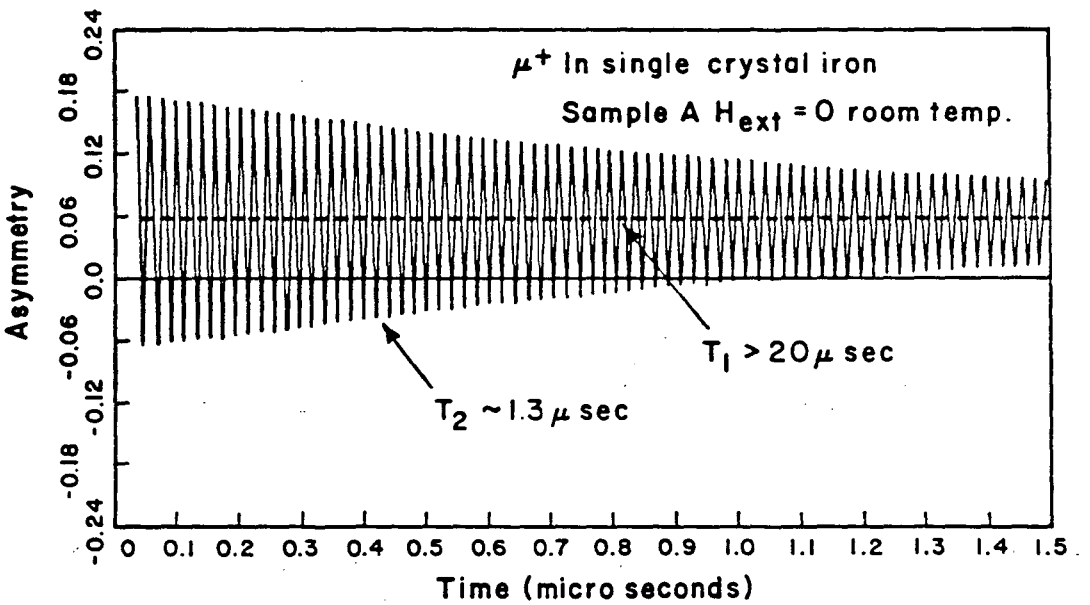
μ+ In single crystal iron
Sample A Hext = 0 room temp.
T1 > 20μ sec
T2 ~1.3μ sec
Asymmetry
0.24
0.18
0.12
0.06
0.0
-0.06
-0.12
-0.18
-0.24
0 0.1 0.2 0.3 0.4 0.5 0.6 0.7 0.8 0.9 1.0 1.1 1.2 1.3 1.4 1.5
Time (micro seconds)

Fig. 24

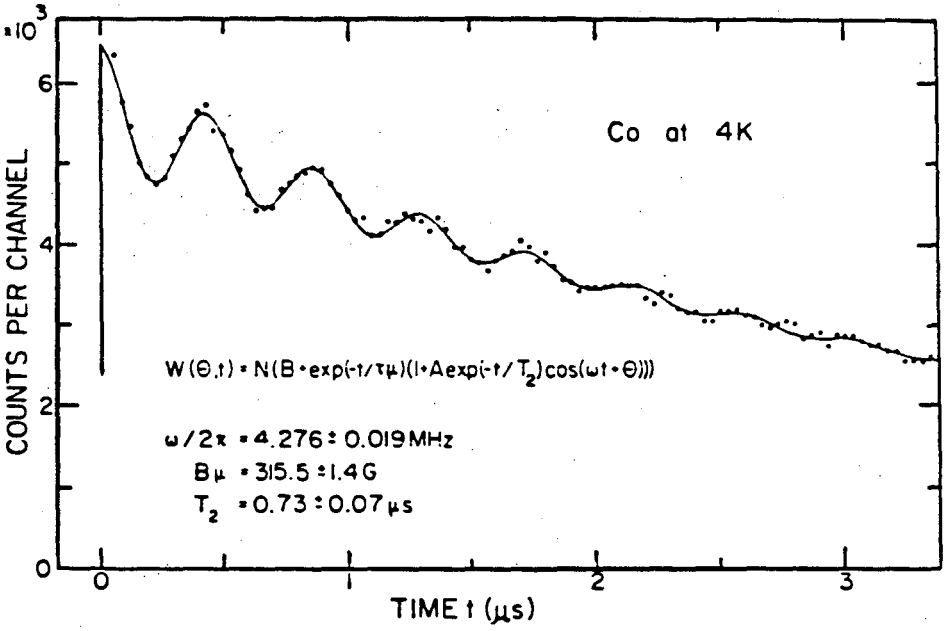
×10³
6
4
2
0
COUNTS PER CHANNEL
Co at 4K
W(Θ,t) = N(B·exp(-t/τμ)(1+Aexp(-t/T₂)cos(ωt+Θ)))
ω/2π = 4.276 ± 0.019 MHz
Bμ = 315.5 ± 1.4 G
T₂ = 0.73 ± 0.07 μs
0
1
2
3
TIME t (μs)

Fig. 25

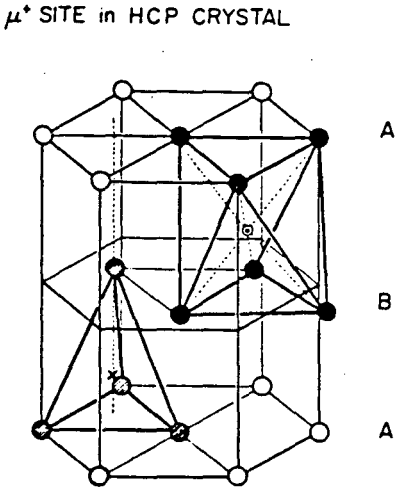
μ⁺ SITE in HCP CRYSTAL
A
B
A
OCTAHEDRAL SITE
TETRAHEDRAL SITE

Fig. 26

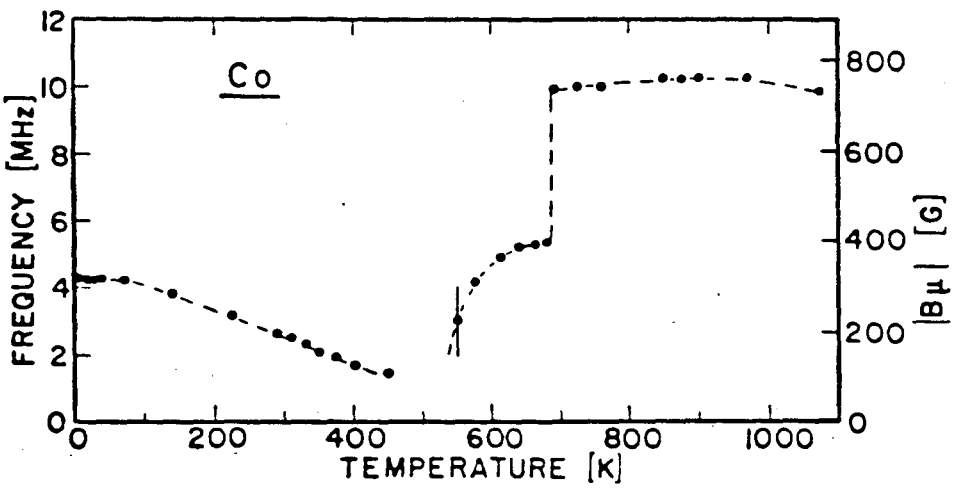
Co
FREQUENCY [MHz]
TEMPERATURE [K]
|Bμ| [G]
0
2
4
6
8
10
12
200
400
600
800
1000

Fig. 27

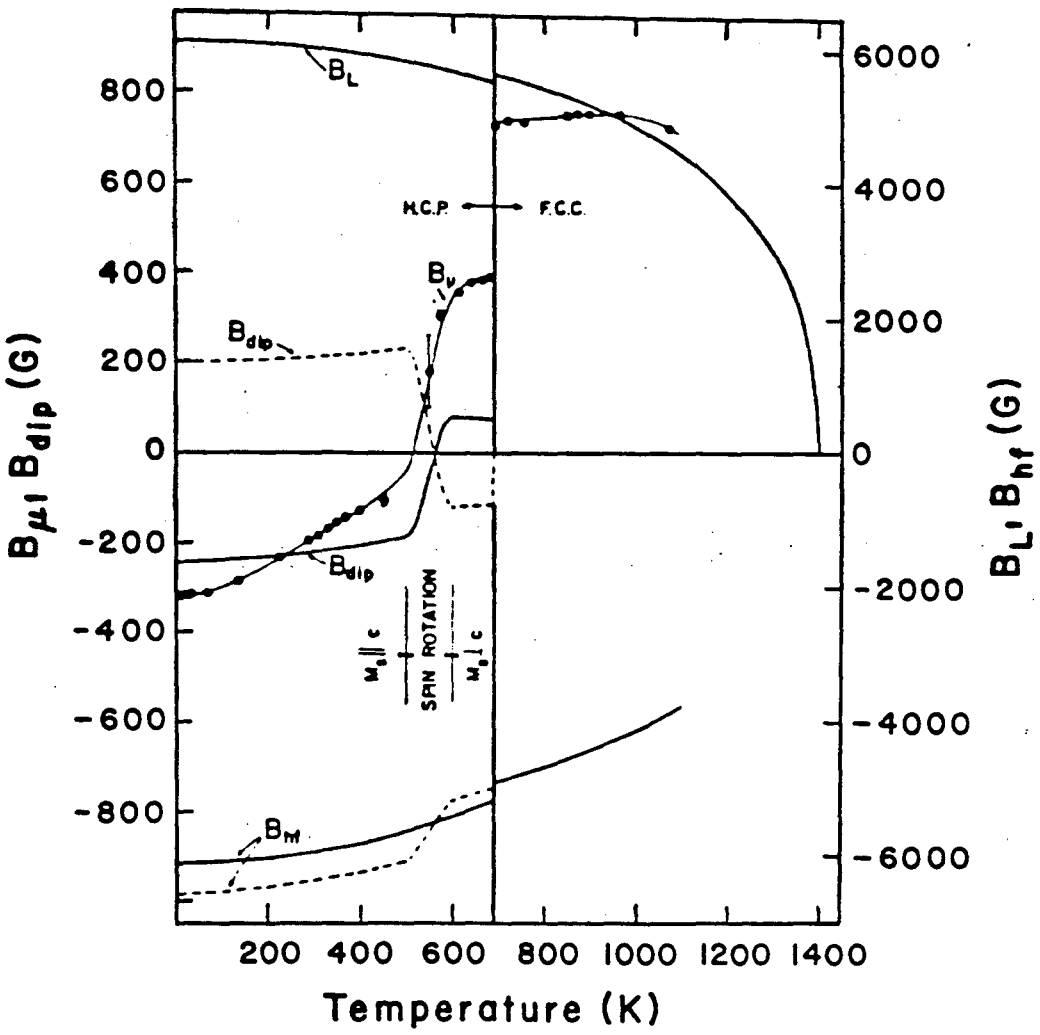
$B_{\mu l}$ B_{dip} (G)
B_L B_{hf} (G)
Temperature (K)
B_L
H.C.P.
F.C.C.
B_v
B_{dip}
B_{dip}
$M_s \parallel c$
SPIN ROTATION
$M_s \perp c$
B_{hf}
800
600
400
200
0
-200
-400
-600
-800
6000
4000
2000
0
-2000
-4000
-6000
200 400 600 800 1000 1200 1400

Fig. 28

This report was done with support from the Department of Energy. Any conclusions or opinions expressed in this report represent solely those of the author(s) and not necessarily those of The Regents of the University of California, the Lawrence Berkeley Laboratory or the Department of Energy.

Reference to a company or product name does not imply approval or recommendation of the product by the University of California or the U.S. Department of Energy to the exclusion of others that may be suitable.

TECHNICAL INFORMATION DEPARTMENT
LAWRENCE BERKELEY LABORATORY
UNIVERSITY OF CALIFORNIA
BERKELEY, CALIFORNIA 94720